Nanoscopic X-ray imaging and quantification of the iron cellular architecture within single fibroblasts of Friedreich's ataxia patients

Bjorn de Samber, Tom Vanden Berghe, Eline Meul, Stephen Bauters, Martin Seyrich, Joél Smet, Boel C de Paepe, Julio Cesar da Silva, Sylvain Bohic, Peter Cloetens, et al.

JOURNAL OF SYNCHROTRON RADIATION
ISSN 1600-5775

Nanoscopic X-ray imaging and quantification of the iron cellular architecture within single fibroblasts of Friedreich's ataxia patients

Björn De Samber,[a,b]* Tom Vanden Berghe,[c,d,e] Eline Meul,[c,d] Stephen Bauters,[f] Martin Seyrich,[g] Joël Smet,[h] Boel De Paepe,[h] Julio Cesar da Silva,[f] Sylvain Bohic,[f] Peter Cloetens,[f] Rudy Van Coster,[h] Peter Vandenabeele[c,d,i] and Laszlo Vincze[a]

[a]Department of Analytical Chemistry, Ghent University, Ghent, Belgium, [b]imec – Vision Lab, University of Antwerp, Wilrijk, Belgium, [c]VIB Center for Inflammation Research, Ghent, Belgium, [d]Department of Biomedical Molecular Biology, Ghent University, Ghent, Belgium, [e]Department of Biomedical Sciences, University of Antwerp, Wilrijk, Belgium, [f]ESRF, Grenoble, France, [g]DESY, Hamburg, Germany, [h]Department of Pediatrics, Division of Pediatric Neurology and Metabolism, Ghent University Hospital, Ghent, Belgium, and [i]Methusalem program, Ghent University, Ghent, Belgium. *Correspondence e-mail: Bjorn.DeSamber@UAntwerpen.be

Received 30 August 2019
Accepted 17 November 2019

Edited by P. A. Pianetta, SLAC National Accelerator Laboratory, USA

Keywords: nano-XRF; Friedreich's ataxia; iron; quantification; imaging.

Friedreich's ataxia (FRDA) is a neurodegenerative disease characterized by an increase in intracytoplasmic iron concentration. Here the nanoscale iron distribution within single fibroblasts from FRDA patients was investigated using synchrotron-radiation-based nanoscopic X-ray fluorescence and X-ray in-line holography at the ID16A nano-imaging beamline of the ESRF. This unique probe was deployed to uncover the iron cellular two-dimensional architecture of freeze-dried FRDA fibroblasts. An unsurpassed absolute detection capability of 180 iron atoms within a 30 nm × 50 nm nanoscopic X-ray beam footprint was obtained using state-of-the-art X-ray focusing optics and a large-solid-angle detection system. Various micrometre-sized iron-rich organelles could be revealed for the first time, tentatively identified as endoplasmic reticulum, mitochondria and lysosomes. Also a multitude of nanoscopic iron hot-spots were observed in the cytosol, interpreted as chaperoned iron within the fibroblast's labile iron pool. These observations enable new hypotheses on the storage and trafficking of iron in the cell and ultimately to a better understanding of iron-storage diseases such as Friedreich's ataxia.

1. Introduction

Friedreich's ataxia or FRDA is an autosomal recessive disorder which is characterized at the cellular level by an accumulation of iron in neuronal cells (Koeppen *et al.*, 2013; Koeppen, 2011; Lamarche *et al.*, 1980). The coordinated distribution of iron between intracellular compartments and the adaptation of iron uptake to intracellular demands are crucial for a balanced iron homeostasis. Iron is an essential metal for the organism because of its unparalleled versatility as a biological catalyst (Andrews, 2008). However, this versatile behavior makes iron acquisition by the organism difficult: at pH 7.4 and physiological oxygen tension, the relatively soluble Fe^{2+} is readily oxidized to Fe^{3+}, which upon hydrolysis forms insoluble ferric hydroxides. As a result of this virtual insolubility and potential toxicity due to redox activity, iron must be constantly chaperoned. When this is not the case, iron becomes a source and an amplifier of reactive oxygen species and is therefore toxic at higher concentrations (Valko *et al.*, 2005; Hassannia *et al.*, 2018; Li *et al.*, 2017; Imoto *et al.*, 2018). FRDA has been coined as a mitochondrial disease since mitochondria take a center stage in cellular iron metabolism;

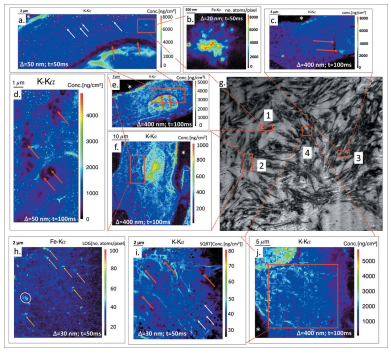

they harbor the two major iron-utilizing pathways – the synthesis of heme and the biogenesis of iron–sulfur (Fe/S) proteins. So-called mitochondrial Fe/S cluster assemblies are essential for the maturation of all cellular proteins with Fe/S co-factors. The abundant iron-dependent proteins known as 'complexes I–IV' also play essential roles in the respiratory chain occurring in mitochondria (Mühlenhoff *et al.*, 2015). Little is known concerning the regulation of iron uptake by the mitochondrion and how this is coordinated with iron metabolism in the cytosol and other organelles such as lysosomes (Kurz *et al.*, 2008). Aconitase, an Fe/S protein involved in iron homeostasis, was found to be deficient in FRDA patients (Rötig *et al.*, 1997). Recent work on FRDA has established that communication does exist between iron metabolism in the mitochondrion and the cytosol; for example, frataxin is a vital protein highly expressed in mitochondria-rich tissues, which has decreased expression in FRDA patients and has been suggested to play several roles: iron storage, chaperone, sensor and/or metabolic switch (Adamec *et al.*, 2000; Bencze *et al.*, 2006, 2007; Bulteau *et al.*, 2004; Cavadini *et al.*, 2002; Cook *et al.*, 2006; Lesuisse *et al.*, 2003). This finding has revealed the ability of the mitochondrion to modulate whole-cell iron processing to satisfy its own requirements for the crucial processes of heme and Fe/S cluster synthesis. Generally, more knowledge of mitochondrial iron processing pathways and the interaction between organelles and the cytosol could revolutionize the investigation of iron metabolism (Richardson *et al.*, 2010).

Synchrotron-radiation-based nanoscopic X-ray fluorescence (SR nano-XRF) – available at few facilities worldwide – is the gold standard for trace-level metal imaging within single cells, nowadays with imaging resolution below 50 nm and, when rigorously performed, in a quantitative manner (De Samber *et al.*, 2016). In the most scrutinized case, SR nano-XRF even allows to determine the number of atoms of a particular element within the area illuminated with the X-ray nanobeam, ultimately providing a 2D elemental map on an atoms per pixel base. Since recently, cryogenic sample environments are also arising at state-of-the-art nanoprobe beamlines, allowing the analysis of vitrified cells close to their native state (Chen *et al.*, 2014). Another powerful aspect of XRF is its sensitivity to the whole pool of a metal considered. For instance, the whole iron pool (*i.e.* all iron species) are probed in the sample, regardless of chemical form and oxidation state. This is generally not the case for chemical staining techniques such as Prussian blue staining (for iron) (Scharlach *et al.*, 2016) or various fluorescent dyes (Ma *et al.*, 2015; Fakih *et al.*, 2009), often only probing free and/or chemically bound elements. Besides simultaneous imaging of biologically relevant metals such as K, Ca, Mn, Fe, Ni, Cu and Zn, non-metalloid biologically relevant elements such as P, S, Cl and Br can also be imaged. This multi-element analytical strength can be used to cross-validate the simultaneous spatial presence (or complementarity) of elements of interest. Besides SR nano-XRF, complementary X-ray imaging methods such as X-ray in-line holography can be deployed in close succession, enabling visualization of the nanoscopic morphology of single cells.

The accumulation of iron has been stated as a hallmark in FRDA; a review describing studies in human tissues and cellular and animal models has recently been provided (Llorens *et al.*, 2019). First observation of intracytoplasmic deposits of iron were found in post-mortem heart samples of all three FRDA patients investigated using Perls Prussian blue staining (Lamarche *et al.*, 1980). In later studies, laboratory-based micro-XRF, slide histochemistry of iron and immunohistochemistry of the two iron-related proteins ferritin and ferroportin have been performed, indicating 1–4 mm^2 regions of significantly increased iron throughout the working myocardium and robust cytosolic ferritin reaction products in many fibres of the affected regions (Ramirez *et al.*, 2012). Laboratory-based micro-XRF, immunohistochemistry, immunofluorescence and lectin affinity fluorescence indicated the redistribution of iron, copper and zinc in the dentate nucleus (Koeppen *et al.*, 2012). Analysis of iron, zinc, copper and calcium of patient tissue using inductively coupled plasma optical emission/mass spectrometry (ICP-OES/MS) identified the decrease of copper in FRDA heart tissue (Kruger *et al.*, 2016). In our previous work (De Samber *et al.*, 2018), we performed quantitative nanochemical imaging of fibroblasts shock-frozen at cryogenic temperatures – as a proxy to neuronal cells – from control and FRDA patients using SR-XRF. We observed clusters of iron-rich hot-spots with similar mass fractions, within the cytoplasm of both control and FRDA fibroblasts. Surprisingly, no significant difference in overall mean iron concentration between control and FRDA fibroblasts was found, but there was a significant decrease in zinc concentration, suggesting metal dysregulation – beyond iron – in cells derived from FRDA patients.

In this study, pioneering chemical imaging of iron upon freeze-dried fibroblasts of FRDA patients was performed at the ID16A X-ray nanoprobe. This one-of-a-kind, high-flux X-ray nanoprobe with state-of-the-art focusing optics and detector geometry is deployed for chemical and morphological imaging of FRDA fibroblasts at the micro- and nanoscopic scale. Relating to FRDA research, SR nano-XRF has the unique capability to examine the iron nanostructure in single FRDA cells, possibly shedding more light on intracellular iron trafficking, iron accumulation and the presence of anomaly iron structures compared with control fibroblasts. Provided the multi-element character that SR nano-XRF delivers, the coinciding presence of other metals/elements in iron-rich regions in FRDA fibroblasts can be tackled as well. In this way, the simultaneous presence of sulfur with iron can be looked at; in particular to confirm the presence of Fe/S clusters in FRDA fibroblasts (Beinert *et al.*, 1997; Johnson *et al.*, 2005).

We analyzed several entire FRDA fibroblasts with moderate spatial resolution of 400 nm, followed by high-resolution scanning down to 20 nm of iron-rich structures. Also, using SR nano-XRF, performing quantitative comparisons between iron structures within and among different FRDA fibroblasts is possible: the main focus of this work was to obtain accurate estimates of surface area, (mean) areal cytoplasm iron concentration and total number of iron atoms

within iron-rich fibroblast microstructures/organelles. Since only parts of fibroblasts were measured, the total iron mass within an entire fibroblast could not be derived from areal concentrations, making comparison of iron concentration with other values obtained by other techniques (*e.g.* ICP-MS) cumbersome. Recently, new methods have been arising where X-ray phase maps can be converted into total areal/volume densities, enabling the conversion of areal concentrations to 3D mass fraction or molar concentrations (Gramaccioni *et al.*, 2018; Yang *et al.*, 2019). In-line X-ray holographic imaging was deployed here as a fast pre-evaluation tool before nano-XRF scanning to verify the preserved morphology of FRDA fibroblasts at the sub-micrometre scale.

2. Methods

2.1. Cell culture

Fibroblasts were taken from FRDA patients at the University Hospital Ghent (UZ Gent, Department of Pediatrics and Medical Genetics) using skin biopsy. The ethics committee of the Ghent University Hospital (UZ Gent) approved the research project and the associated collection of skin biopsies. The research was declared to the Commission for the Protection of Privacy (CPP, Belgium). Skin biopsies from FRDA patients were collected with prior consent of patients and no money was exchanged in whatsoever form to collect the samples. After skin biopsy, human fibroblasts were further cultured in Opti-MEM medium supplemented with 1% L-glutamine solution, 1% penicillin streptomycin solution and 12.5% fetal bovine serum and kept in an incubator at 37°C and 5% CO_2. Silicon nitride (Si_3N_4) wafers (from Silson Ltd, Northampton, UK) are established supports for XRF analysis due to their ultra-purity and low thickness. Silicon nitride wafers (5 mm × 5 mm size, 1.5 mm^2 membrane area, 500 nm membrane thickness and 200 µm frame thickness) were removed from their gelatin capsule container using tweezers, washed twice in 70% ethanol (Molecular Biology Grade, Fisher BioReagents) to sterilize and washed twice in ultrapure water (Milli-Q, Merck Millipore) by brief submersion. Silicon nitride wafers were then deposited in µ-Slide 8 Well Chamber Slides (ibidi, Germany), followed by immediate seeding of fibroblasts. After incubation, resulting in firm attachment and growing of the fibroblasts verified by optical microscopy, Opti-MEM cell culture medium was removed, and the wafers were briefly washed in 0.25 *M* freshly prepared ammonium formate solution (3.1538 g ammonium formate, Optima LC/MS grade from Fisher Chemical, dissolved in 200 ml milli-Q water) to remove the medium, containing salts and trace-level metals.

2.2. Cryofixation, freeze-drying and carbon-coating

As vitreous ice upon the fibroblasts causes X-ray absorption, excess ammonium formate washing solution was removed via blotting just before the plunge-freezing procedure. Due to the unavailability of commercial plunge-freezing equipment, Si_3N_4 wafers were plunge-frozen manually in liquid isopentane, which was cooled down to −150°C using liquid nitrogen. After plunge-freezing, the excess of liquid isopentane on the wafers was removed via blotting with absorbing paper which was precooled in the cold air above the liquid-nitrogen bath. Wafers were then further cooled down to liquid-nitrogen temperature by immersion in liquid nitrogen and stored in cryogenic vials. Fibroblast cells that were measured under cryogenic conditions were kept as such until analysis. Fibroblast cells intended for analysis under ambient temperature were transferred in liquid nitrogen to a freeze-dryer and were freeze-dried for 48 h. For our experiments, we used both an in-house-built freeze-dryer provided at the Department of Pharmaceutics, and a commercial freeze-dryer (Christ, Germany) provided at the Department of Chemistry, Ghent University, Belgium. After completion of the freeze-drying process, wafers with freeze-dried fibroblasts were coated with a 10 nm carbon layer using a Leica EM ACE600 to reduce sample radiation damage.

2.3. ID16A 'nano-imaging' beamline

The X-ray beam size during our experiment was estimated to be 30 nm (horizontally) × 50 nm (vertically) full width at half-maximum (FWHM) at an excitation energy of 17.1 keV by means of knife-edge scans on a test pattern developed by Minatec (Grenoble, France). In high-dose mode – equivalent to a 50 µm secondary source opening – the X-ray flux was determined to be 1.5×10^{11} photons s^{-1}; low-dose mode corresponds to a 10 µm secondary source opening. Although always performed under high-vacuum conditions, the ID16A experiment can be operated in cryogenic or 'non-cryogenic mode'. Both modes are not interchangeable within one beam time due to time constraints. In this work, for the analysis of freeze-dried cells, the non-cryogenic mode was deployed. In this mode, a load-lock with up to 16 sample positions is available and a gripper can be deployed, enabling an in-vacuum sample change. At the time of measurement, the experiment chamber was equipped with a dual detector configuration, composed of two arrays of six single SDD detectors nicknamed 'William' and 'Harry' (Rayspec Ltd, UK). Both detector arrays – containing 12 SDDs in total – approach the sample from two sides, enabling collection of XRF over a larger total solid angle, also providing mutual shielding from background fluorescence and Compton scattering. The composition of both array detectors was different in the sense that Harry has a vertical SDD configuration (two columns with three rows, positioned on the left-hand side when looking downstream, XIA channels 0–5), whereas William has a horizontal SDD configuration (two rows of three columns, positioned on the right-hand side when looking downstream, XIA channels 8–11). All 12 detectors with 2048 channels produce a data output of approximately 80 Mb s^{-1} for an acquisition time of 50 ms in scanning mode. An ESRF FReLoN camera (2000 × 2000 pixels) was used for performing X-ray in-line holography. X-ray holograms were collected in the Fresnel region at four different distances, located approximately 10 mm behind the X-ray nano-focus. To obtain the highest density sensitivity, a specific acquisition grid

enabled the removal of spurious contrast on the holograms introduced by the Kirkpatrick–Baez focusing mirrors. For each distance, the average image was taken of 17 different lateral positions of the sample to eliminate cross-talking between the illumination structures and the sample. Phase retrieval was performed using ESRF in-house-developed algorithms and software (Fus *et al.*, 2018). The pixel size in the reconstructed phase-contrast images corresponds to a 25 nm distance; the total obtained field-of-view is 50 µm × 50 µm. Additional technical information on the ID16A experiment, as well as a technical description of the experiment layout, can be found elsewhere (Cagno *et al.*, 2017; da Silva *et al.*, 2017).

2.4. Determination of the limits of detection

Elemental limits of detection (LODs) were determined by measuring an AXO thin film XRF reference sample (RF-200-S2371; AXO Dresden GmbH) and NIST SRM 1577C (bovine liver powder). The powder was pressed into a self-supporting pressed pellet (thickness approximately 100 µm, diameter 13 mm, areal mass 16.2 mg cm^{-2}). For XRF analysis, a thin flake was cut from the pellet using a razor blade. For NIST SRM 1577C, an area of 4.95 µm × 4.95 µm was scanned with 50 nm steps and 50 ms dwell time (100 × 99 points, 495 s measuring time); for the AXO, a 9.95 µm × 9.95 µm area with 50 nm steps and 50 ms dwell time (199 × 199 pixels, 1990 s measuring time). From both measurements upon NIST SRM 1577C and AXO thin film standard, an XRF sum spectrum was made, which was then normalized to 1 s measuring time, 200 mA ESRF ring current and corrected for dead-time. Since the I_0 signal was unavailable and I_t is subject to sample thickness, the ESRF ring current was used as the normalization signal (also good linearity was observed between I_t and ESRF ring current). Note that, due to a detector dead-time above 50%, both standards were measured in low-dose mode (10 µm secondary source opening instead of 50 µm, implying a factor of five lower flux) and an additional 4.6 µm thin gold absorber (factor of 3.1 lower flux). In order to make the LODs representative for the conditions under which the samples are measured (high-dose mode and no absorbers), elemental intensities obtained from both standard reference materials (SRMs) were multiplied by a factor of 5 and 3.1 (*i.e.* 15.5 times in total). Normalized XRF sum spectra were then fitted using *AXIL* (*Advanced X-ray analysis using Iterative Least-Squares*) (Vekemans *et al.*, 1994), providing the net peak and background intensity, I_{net} and $I_{background}$. The LOD of a specific element i can then be determined by using the following formula,

$$\mathrm{LOD}_{\mathrm{relative},i} = \frac{A_{\mathrm{corr},i}(\mathrm{SRM})}{(\rho d)_{\mathrm{SRM},i}} \frac{\sqrt{I_{\mathrm{background},i}}}{I_{\mathrm{net},i}} \omega_i , \qquad (1)$$

where $A_{\mathrm{corr},i}$(SRM) denotes the absorption correction factor for element i for the SRM used (expressed in g cm^{-2}), $(\rho d)_{\mathrm{SRM},i}$ is the areal concentration of element i in the SRM (also in g cm^{-2}) and ω_i is the certified mass fraction of element i in the SRM used,

$$A_{\mathrm{corr},i}(\mathrm{SRM}) = \frac{1 - \exp\left[- \chi_{\mathrm{SRM}(i)} (\rho d)_{\mathrm{SRM}(i)} \right]}{\chi_{\mathrm{SRM}(i)}}, \qquad (2)$$

where $\chi_{\mathrm{SRM}(i)}$ represents the absorption correction factor of element i for the used excitation energy and SRM, calculated according to the fundamental parameter method; more information is provided in earlier work (De Samber *et al.*, 2018). For our specific case the absorption correction factor for iron in NIST SRM 1577C was determined to be 0.85, assuming a fixed angle of 90° between X-ray beam and sample surface and a 17° angle between sample surface and detector. For the AXO thin film standard, no self-absorption factor was required since mass depositions are in the ng cm^{-2} range, equivalent to only a few atomic layers. Note that in equation (1), $A_{\mathrm{corr},i}$(SRM) is additionally divided by $(\rho d)_{\mathrm{SRM}}$; since χ_{SRM} is expressed in cm^2 g^{-1} and $(\rho d)_{\mathrm{SRM}}$ is expressed in g cm^{-2}, the expression for the relative LOD becomes dimensionless. For calculating χ_{SRM} in equation (2), the angle between the incoming X-ray beam and sample surface was fixed at 90°; the (average) angle between sample surface and detector was estimated to be 17°. By replacing ω_i with $(\varphi d)_{\mathrm{SRM}(i)}$, areal LODs can be obtained. By further complementing the formula with beam size, molar weight M_g and Avogadro's number N_A, the absolute, molar and atomic LODs are obtained, respectively. The horizontal and vertical beam size for the LOD calculations was estimated to be 30 nm × 50 nm FWHM.

2.5. XRF quantification procedure

Elemental yields were determined for the AXO thin film standard and NIST SRM 1577C in counts/(atom/pixel)/s, including a geometry-dependent self-absorption correction for NIST SRM 1577C as provided in equation (2). For typical scanning mode (50 ms dwell time), a corresponding elemental yield of 0.010 counts/(atom/pixel)/50 ms was obtained for iron from NIST SRM 1577C and 0.089 counts/(atom/pixel)/50 ms for iron from the AXO thin film standard (self-absorption correction was considered negligible for the latter). Next, XRF elemental maps were batch-processed in simultaneous multi-processing mode using the in-house-written software *MICROXRF* (written in IDL; Harris Geospatial Solutions) and normalized to 1 s measuring time, ESRF ring current (200 mA) and corrected for dead-time. Although normalization of XRF spectra is generally performed by measuring beam intensity using sensitive calibrated diodes, data were normalized to the ESRF ring current for the following reasons: (i) the beam intensity I_0 measured before the sample showed a high noise signal, (ii) the beam intensity behind the sample I_t signal varied significantly with sample (ice) thickness and also between sample and standard, and (iii) good linearity between ESRF ring current and I_t was observed within a single XRF map.

The obtained normalized elemental maps were then background-corrected using the normalized mean intensity of the so-called 'background' cluster defined outside the fibroblast cell. As such, background fluorescence originating from the

sample chamber can be efficiently removed from the elemental maps. When no background area was available within the same map, mean background intensity was calculated from the coarse (400 nm) overview map; background cluster area was always selected a few micrometres away from the fibroblast cell membrane to avoid 'stray' fluorescence from the cell. Freeze-dried fibroblasts deposited onto the silicon nitride membranes can be considered quasi-transparent for X-ray fluorescence since the silicon (K_α) elemental map of the silicon nitride membrane did not show any signs of X-ray fluorescence absorption by the freeze-dried cell deposited on top of it. Finally, areal concentration maps of the fibroblast cells were obtained by dividing the normalized elemental maps by the elemental yields derived from the SRMs.

Note that for quantification of cryofrozen fibroblasts [shown later in Fig. 5(*e*)], additional self-absorption correction of the ice layer covering the cell was included. For estimating the thickness of the ice layer covering the cell, the K-K_α/K_β ratio of the sum spectrum of the entire map can be used, providing the following formula for the ice layer thickness,

$$T\ (\mu\text{m}) = \log\left[\frac{\left(K_\alpha/K_\beta\right)/R_0}{-\left(\mu_{K_\alpha} - \mu_{K_\beta}\right)}\right] \times (1 \times 10^4)\ \sin(\beta). \quad (3)$$

The resulting absorption correction factor $A_{\text{corr},i}$(SRM) for the ice for a specific element i is provided by

$$A_{\text{corr, ice}} = 1/\chi_{\text{ice}}(i)\,(\rho d)_{\text{ice}}. \quad (4)$$

In equation (4), the areal ice thickness $(\rho d)_{\text{ice}}$ is typically expressed in g cm^{-2} and can be obtained by dividing the thickness of the ice layer (expressed in µm) by a factor of 1×10^4, when assuming an ice density of approximately 1 g cm^{-3}. Additional details on the normalization and quantification procedure can be found in previous work (De Samber *et al.*, 2018). Calculation of the number of atoms per pixel in the elemental maps was performed using the following equation,

$$\frac{\text{No. atoms}}{\text{pixel}} = c_{\text{areal}}\left[\frac{\text{g}}{\text{cm}^2}\right] p_x\, p_y\,[\text{cm}^2] \,/\, M_{\text{g}}\left[\frac{\text{g}}{\text{mole}}\right] N_{\text{A}}\left[\frac{\text{atoms}}{\text{mole}}\right], \quad (5)$$

where c_{areal} denotes the obtained areal concentration in the elemental map, $p_x p_y$ the area of a single pixel (corresponding to the step size), M_{g} the molar mass of the element considered and N_{A} Avogadro's number. Manual clustering of iron-rich regions resulted in a quarter increase of the mean surface area compared with automatic K-means clustering; this is likely caused by the manual selection of the pixels belonging to the imaged iron-rich structures, resulting in a larger selected cluster area. For calculating the total number of atoms within an iron hot-spot, manual clustering based upon individual pixel selection in the iron map was therefore preferred above automatic K-means clustering. Summing the values of all pixels forming the iron cluster then directly provides the total number of iron atoms in the cluster. The mean areal iron concentration can be derived from the total amount of iron determined in the cluster and its surface area,

$$c_{\text{areal}}(\text{Fe}) = \frac{\text{No. atoms}}{N_{\text{A}}\, M_{\text{g}}} \,/\, \left[p_x\, p_y \times \text{No. pixels}\right]. \quad (6)$$

In the same manner, the mean areal concentration of the cytosol can be derived by using the complementary cluster area. This enables estimating the ratio of the mean areal concentration of the background with respect to the mean areal concentration of the iron particle.

3. Results and discussion

3.1. Limits of detection and considerations on quantitative XRF analysis

To enable trace-level nano-imaging in freeze-dried human FRDA fibroblasts, we used the ID16A 'nano-imaging' beamline located at the ESRF in Grenoble, France. It provides a unique combination of high flux, *i.e.* 2×10^{11} photons s^{-1}, and nanoscale resolution, *i.e.* 30 nm × 50 nm. A typical XRF sum spectrum of (i) a 500 nm-thick 'blank' Si_3N_4 membrane, (ii) NIST SRM 1577C, (iii) AXO thin film, (iv) an entire FRDA fibroblast and (v) an iron-rich hot-spot, all normalized to 100 s measuring time, is provided in Fig. 1(*a*). Note that the presence of nickel in the XRF spectrum of the 'blank' Si_3N_4 membrane is caused by the presence of a Ni test pattern on the wafer. From the XRF spectra of NIST SRM 1577C (bovine liver) and AXO thin film, acquired in non-cryogenic mode, LODs were extrapolated for typical scanning conditions used for scanning cells [*i.e.* no absorbers in the beam, high-dose mode (50 µm opening of the secondary source) and a dwell time of 50 ms], which are provided in Fig. 1(*b*) and Table 1. The deployed experimental setup achieved relative limits of detection in NIST SRM 1577C 'bovine liver' for iron of 1.1 p.p.m. in scanning mode. Assuming a 30 nm (horizontal) × 50 nm (vertical) X-ray beam size (FWHM), the areal LOD is equivalent to 17 ng cm^{-2} iron, corresponding to an absolute LOD of 0.26 ag (attogram or 10^{-18} g) of iron, or 2800 iron atoms. When approximating the density of NIST SRM 1577C to 1 g cm^{-3}, molar LODs of 19 µM iron can be derived. Additionally, LODs were also determined from an AXO thin film standard, which can be considered as an idealized absorption-free standard with only few atomic layers deposited. When assuming a total areal mass of 3.7 ng cm^{-2} for the AXO thin film standard (including all atomic layers of Pb, La, Pd, Mo, Cu, Fe and Ca), relative LODs of 0.3 p.p.m. (300 p.p.b.) are obtained for iron, equivalent to 1.1 ng cm^{-2}, 17 zg (zeptogram or 10^{-21} g) or only 180 iron atoms, approaching the spatially resolved detection of single atoms. These lower LODs of the AXO thin film compared with the NIST SRM 1577C standard are likely due to the higher thickness of the latter (approximately 70 µm), causing increased scatter and therefore increased background signal, negatively influencing the achievable LOD value. Since freeze-dried cells are much more similar to the AXO thin film standard in terms of scattering properties, the achieved LODs for iron in freeze-dried fibroblasts approach a similar detection level. More information on the calculation of LODs can be found in Section 2.4.

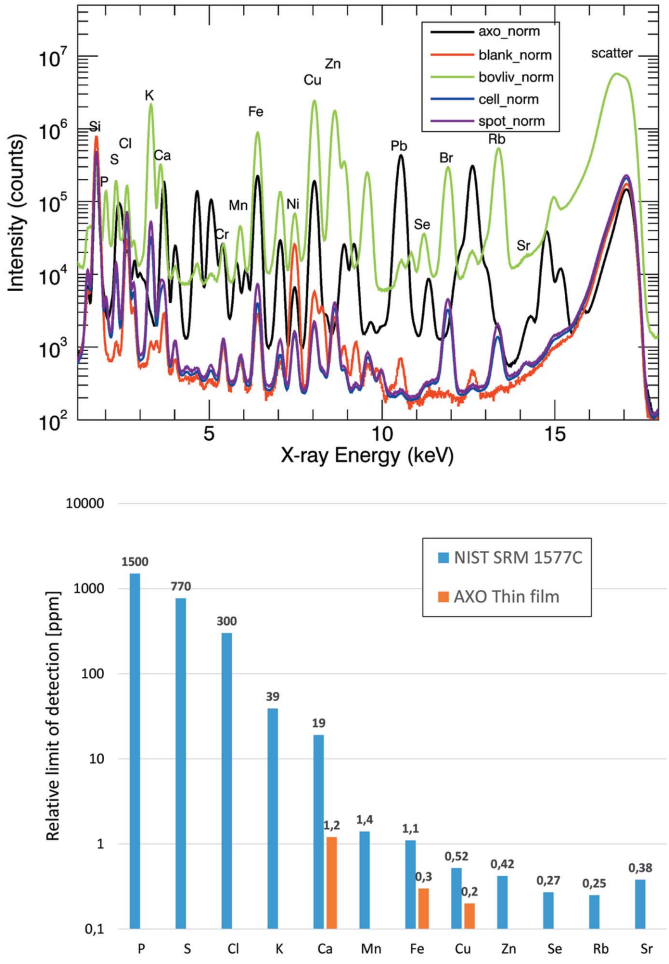

Figure 1
(*a*) XRF sum spectrum of AXO thin film standard (black curve), Si_3N_4 membrane of 500 nm thickness of 'minatec test structure' (green curve), pressed pellet of NIST SRM 1577C (16.2 mg cm^{-2}, black curve), entire fibroblast shown in Fig. 4 (blue curve), iron hot-spot shown in Fig. 4(*g*). All spectra were normalized to 100 s measuring time, no absorbers and high-dose mode. (*b*) Relative detection limits of NIST SRM 1577C (bovine liver) and AXO thin film for experimental conditions typically used for cell scanning (high dose, no absorber, 50 ms dwell time).

The presence of iron in the blank XRF spectrum shown in Fig. 1(*a*) – caused by scattering and fluorescence from the sample environment – stresses the absolute need for background-correction during quantification. Since the AXO thin film standard features negligible self-absorption – just like the freeze-dried fibroblast cell monolayers – its iron elemental yield [0.0890 counts/(atom/pixel)/50 ms] was used for quantification of the iron fibroblast elemental maps. Compared with the pressed pellet of NIST SRM 1577C, the AXO thin film standard also features higher accuracy in terms of areal concentrations. For quantification (in ng cm^{-2}) of all other elements (P, S, Cl, K, Ca, Mn, Ni, Cu, Zn and Br) not present in the AXO thin film, (self-absorption-corrected) elemental yields obtained with the NIST SRM 1577C were used, which are provided in Table 1. Under cryogenic conditions, only NIST SRM 1577C standard was measured since the AXO standard has a much higher risk of breaking when plunge-freezing and subsequent mounting under cryogenic conditions. Since NIST SRM 1577C features higher scattering and background compared with the AXO thin film standard, lower 'virtual' elemental yields and higher LODs are derived from it. Therefore, the iron elemental yield derived from NIST SRM 1577C measured under cryogenic conditions was multiplied by the ratio of the elemental yield of iron in the AXO and NIST SRM, both measured under non-cryogenic conditions.

3.2. SR-XRF analysis of FRDA fibroblasts

3.2.1. SR nano-XRF scanning of freeze-dried versus cryofrozen cells. Analysis of cryofrozen cells close to the native state can be considered as the most trustworthy approach since structural damage, movement of organelles and amassment of dissolved metals in the cytosol is minimal. However, in our study, analysis of freeze-dried fibroblasts under ambient temperature was performed instead of analysis of cryogenically frozen fibroblasts (De Samber *et al.*, 2018). Although freeze-drying of single cells can cause more structural defects compared with vitrification, no chemical intervention whatsoever is applied during freeze-drying, ensuring appropriate chemical preservation of the cell; this in contrast to chemical fixation techniques (Jin *et al.*, 2017). Note that XRF imaging is sensitive for the whole cellular iron pool, *i.e.* both Fe^{2+} and Fe^{3+}; both for freeze-dried and cryofrozen samples the majority is likely Fe^{3+}, although (reducing) conversions may arise due to the high X-ray flux (to a lesser extent for cryofrozen samples).

Several compelling benefits promoted analysis of freeze-dried fibroblasts under non-cryogenic conditions. First, freeze-dried cells can be easily transported, optically characterized and are less stringent in terms of biosafety regulation compared with cryofrozen cells. Second, freeze-dried cells are less sensitive to radiation damage due to their low total mass and absence of water. In order to still minimize radiation damage upon freeze-dried FRDA fibroblasts, cells were coated with a 10 nm layer of carbon (see Section 2.2 for more information). This renders the samples more conductive, dissipating electric charging effects during XRF scanning and reducing sample radiation damage. Practically, freeze-dried fibroblasts generally showed a slight darkening in the optical microscopy image after repeated scans on the same area, but generally nearly identical metal distributions were obtained. However, on one single event we observed a 'bubble' appearing on the sample surface, with growing diameter up to 100 µm, likely related to the carbon coating. Third, due to their lower sensitivity to radiation damage, freeze-dried fibroblasts could also be measured under ambient temperature, providing the additional side-advantage of fast sample change for our specific set-up: a total of 16 samples can be introduced in the ID16A nanoprobe load-lock at once which is then brought to high-vacuum. Sample change between all 15 loaded samples can then be effected in less than 15 min, which is a critical factor when analysis of a large number of sample wafers is envisaged. Fourth, compared with cryofrozen cells, freeze-dried cells do not contain an ice matrix and are also not covered by an additional protective ice layer. This ice gener-

Table 1
Limits of detection (LODs) obtained in NIST SRM 1577C (bovine liver) and AXO thin film standard in non-cryogenic mode.

LODs are expressed in relative (p.p.m.), areal (ng cm^{-2}), absolute (ag), atomic (number of atoms) and micromolar (μM) units. Total areal mass for each standard is provided at the top. For all LOD calculations, the following parameters were valid: no absorbers in the beam path, high-dose mode (50 µm secondary source opening) and a dwell time of 50 ms, which are all typical parameters used for scanning single cells.

NIST SRM 1577C 'bovine liver' (ρd = 16.2 mg cm^{-2})

Element	Certified mass fraction (p.p.m.)	Relative LOD (p.p.m.)	Areal LOD (ng cm^{-2})	Absolute LOD (ag)	Atomic LOD (No.)	Molar LOD (μM)	Elemental yield (counts/atom/50 ms)
P	11750	1500	24000	350	6.9×10^6	4.7×10^4	1.4×10^{-5}
S	7490	770	12000	190	3.5×10^6	2.4×10^4	5.5×10^{-5}
Cl	2870	300	4800	73	1.2×10^6	8.4×10^3	1.6×10^{-4}
K	10230	39	640	9.6	1.5×10^5	1.0×10^3	6.4×10^{-4}
Ca	131	19	310	4.6	6.9×10^4	4.8×10^2	1.5×10^{-3}
Mn	10.5	1.4	23	0.340	3.7×10^3	25	1.3×10^{-2}
Fe	**198**	**1.1**	**17**	**0.260**	$\mathbf{2.8 \times 10^3}$	**19**	$\mathbf{1.7 \times 10^{-2}}$
Cu	275	0.52	8.4	0.130	1.2×10^3	8.1	4.0×10^{-2}
Zn	181	0.42	6.9	0.100	950	6.5	4.4×10^{-2}
Se	2.0	0.27	4.4	0.067	510	3.5	8.1×10^{-2}
Rb	35	0.25	4.0	0.060	420	2.9	9.9×10^{-2}
Sr	0.095	0.38	6.2	0.093	640	4.4	8.8×10^{-2}

AXO thin film standard (ρd = 3.7 ng cm^{-2})

Element	Certified mass fraction (ng mm^{-2})	Relative LOD (p.p.m.)	Areal LOD (ng cm^{-2})	Absolute LOD (ag)	Atomic LOD (No.)	Molar LOD (μM)	Elemental yield (counts/atom/50 ms)
Ca	11.4	1.2	4.5	0.07	1000	112	2.5×10^{-2}
Fe	**3.9**	**0.30**	**1.1**	**0.017**	**180**	**20**	$\mathbf{1.5 \times 10^{-1}}$
Cu	2.0	0.20	0.7	0.011	110	12	2.6×10^{-1}
Pd	1.5	3.0	11	0.17	950	105	2.8×10^{-2}
La	11.7	1.4	5.1	0.08	330	37	8.5×10^{-2}
Pb	7.6	0.31	1.2	0.02	50	5.6	7.1×10^{-1}

ates more X-ray scattered photons (Compton and Rayleigh scattering), exciting the surrounding sample chamber and leading to increased background signal. Achievable LODs that can be obtained within freeze-dried cells are therefore better than those obtained in cryofrozen cells. Fifth, the removal of the water matrix within freeze-dried cells and the absence of a (protective) water layer above the cells compared with analysis of cryofrozen cells simplifies the quantification procedure, as well as the detection of lower atomic number elements (P, S, Cl), *e.g.* when the ice layer reaches 30 µm thickness, phosphorus fluorescence is attenuated completely. The protective ice layer obtained by blotting and succeeding plunge-freezing required for cryo-analysis can vary significantly (from below 1 µm up to 100 µm). Self-absorption corrections for trace metals within the ice matrix are possible, but may induce more variations in the results. Provided these advantages of analysis of freeze-dried cells, it should nevertheless be underscored that, in cases with lower sample throughput, analysis of cryofrozen fibroblasts covered with thin ice (<10 µm) in combination with optimized detector geometry is still the 'spearhead' method as it maintains the elemental distributions within cells as close as possible to the native state.

3.2.2. Nanoscale elemental imaging of FRDA fibroblasts. Elemental distributions within entire fibroblasts were first obtained at (sub)microscopic resolution (1 µm to 200 nm resolution), followed by nanoscopic analysis (200 nm to 10 nm) of regions of interest with higher (sub-p.p.m.) sensitivity. In total, three silicon nitride membranes with FRDA fibroblasts were analyzed. A total of up to ten coarse scans (400 nm pixels) were acquired per wafer, after which detailed scans (50 nm pixel size) were performed upon single fibroblasts, resulting in a total of six high-quality nano-XRF maps on single fibroblasts. Additionally, even higher resolution maps (down to 10 nm pixel size, longer measuring time) were acquired upon iron-rich nanoscopic structures, resulting in several dozen elemental maps of iron-rich regions within FRDA fibroblasts. Fig. 2 illustrates the unique capability of elemental imaging of a large number of fibroblasts cells at different length scales (also referred to as 'zoom' imaging). Due to its overall presence in the fibroblast cytosol and the high signal-to-noise ratio of potassium, potassium clearly depicts the overall freeze-dried fibroblast morphology: cell border, nucleus and (fibrous-like) cytoplasm can be clearly distinguished. From the coarse potassium maps shown in Figs. 2(*e*), 2(*f*) and 2(*j*), regions containing a significant portion of the fibroblast cytoplasm were re-scanned at higher resolution (30 nm or 50 nm step size), resulting in high-resolution elemental distributions provided in Figs. 2(*a*), 2(*d*) and 2(*i*). Besides the droplet-structure in the potassium elemental maps [likely caused by some kind of aggregation of potassium during the freeze-drying procedure (Herrera *et al.*, 2013)], we can also observe a foamy sponge-like structure associated with hollow spaces. [This is indicated with red arrows in Figs. 2(*d*) and 2(*i*). This phenomenon may be caused by deposition of potassium upon inner structures of the fibroblast (*e.g.* cytoskeleton) during the freeze-drying procedure. Within the high-resolution (50 nm pixel size) XRF map in Fig. 2(*a*), a rather complex iron-rich structure was found, which was re-scanned with 20 nm pixel size, shown in Fig. 2(*b*).] Note that in Fig. 1(*a*) the relative iron increase in the XRF sum spectrum series (i) blank membrane, (ii) fibroblast cell, (iii) iron 'hot spot' is also clearly visible. Iron nanostructures were also present in Fig. 2(*h*), among which a worm-shaped structure (circled in white) and several iron hot-spots (indicated with yellow arrows). Due to the extremely low masses of iron present, *i.e.* a few thousand atoms/pixel, areal concentrations are depicted in number of iron atoms per pixel rather than in ng cm^{-2}. This confirms the capability of SR nano-XRF of visualizing iron-containing structures within human FRDA fibroblasts at the nanoscale.

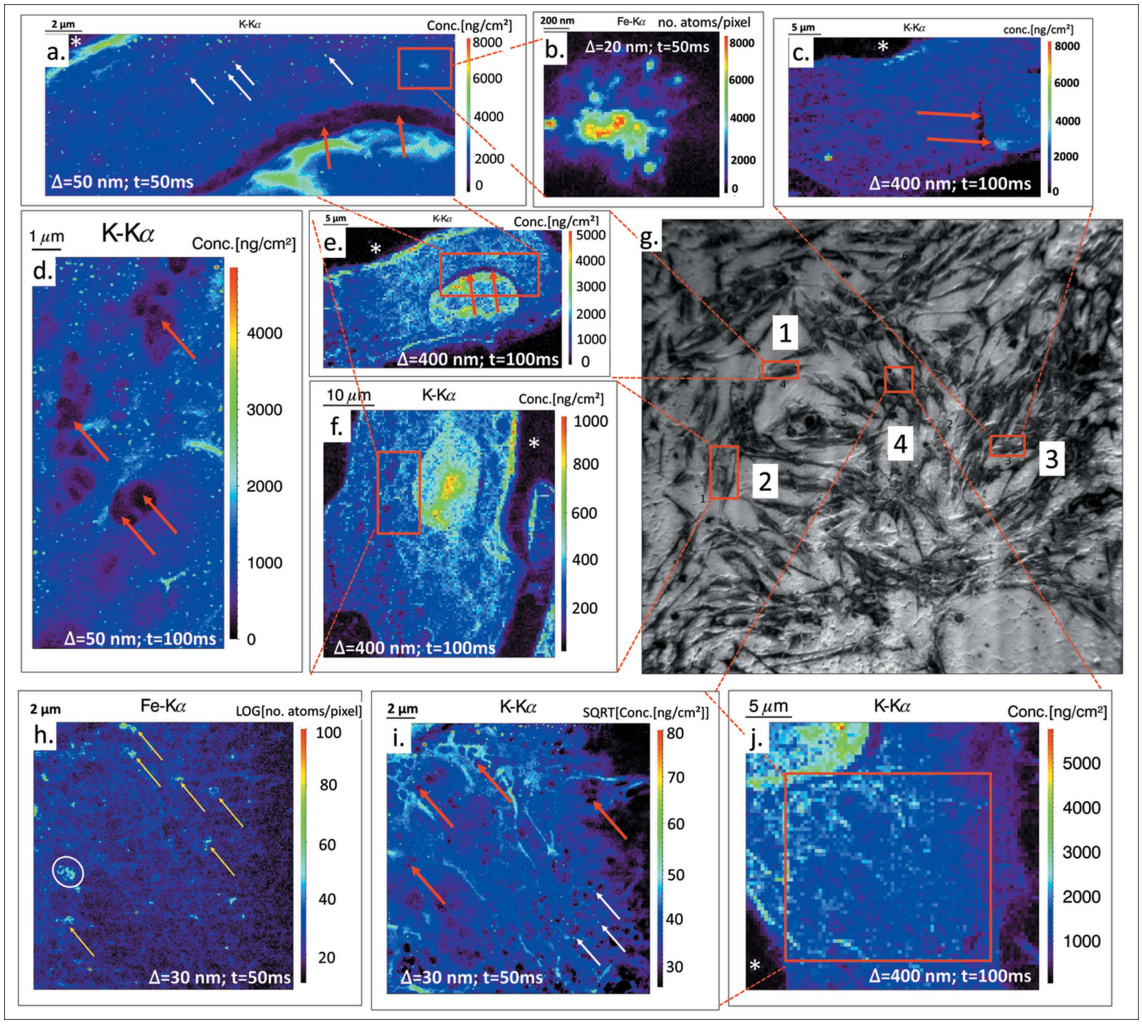

Figure 2
Multi-scale imaging of FRDA fibroblasts at the sub-micrometre and nanoscopic scale. (*a*) Potassium distribution of fibroblast nucleus and cytoplasm in 'fine' mode (50 nm pixel size). (*b*) Iron distribution of subarea in (*a*) imaged with 20 nm pixel size. (*c*), (*e*) and (*f*) Potassium elemental distribution of fibroblasts scanned in 'coarse' mode (400 nm pixel size). (*d*) Porous structure of the freeze-dried fibroblast; red arrows indicate hollow areas. (*g*) Light microscopy image of freeze-dried FRDA fibroblasts as observed inside the ID16A nanoprobe; red rectangles indicate the fibroblast cells which were selected for 2D XRF scanning. (*h*) and (*i*) Iron and potassium elemental distribution in the fibroblast cytoplasm with 30 nm pixel size. The white oval and arrows and in (*h*) indicate the presence of iron-rich regions. All areal concentrations are background-corrected. The asterisks (*) indicates regions which were used for background subtraction. Areal elemental concentrations of potassium are provided in ng cm^{-2}; areal elemental concentrations of iron are provided in number of atoms/pixel. Quantification for iron was based upon an AXO thin film standard and upon NIST SRM 1577C for all other elements. For each elemental map, step size (Δ) and dwell time (*t*) are indicated. Note that in the case of a large, non-linear spread of elemental intensities, elemental maps were the square-root or logarithm [as in (*i*) and (*h*), respectively]; this generally provides a better spread of intensity values across the color scale.

Quantitative XRF analysis was performed upon this iron-rich structure, for which the results are summarized in Table 2 (first line). By means of cluster analysis, the iron-rich structure was estimated to have a surface area of 0.7–1.1 μm^2 and to contain approximately four to five million iron atoms. The Pearson correlation coefficient of the iron and sulfur elemental map was 0.33, indicating little correlation between both elemental maps.

Fig. 3 displays five peculiar iron structures detected within other FRDA fibroblasts: Fig. 3(*a*) looks rather spherical and may represent iron-rich lysosomes, Fig. 3(*b*) shows a rather elongated shape, Fig. 3(*c*) reveals a curl-like iron-rich shape, which recalls the circled mitochondrion-like structure shown earlier in Fig. 2(*h*) [shown enlarged in Fig. 3(*d*)]. It has an approximate diameter of 1 μm, strongly matching the size of a mitochondrion (Lackner, 2013), for which a mean diameter of approximately 0.5–1 μm is provided in the literature (Wiemerslage & Lee, 2016). Its curl-shape also strongly resembles the mitochondrion matrix, known to contain two-thirds of the total mitochondrion protein content. Absolute confirmation of the mitochondrial identity was not possible since transmission electron microscopy of entire freeze-dried fibroblast is not feasible. Although fluorescent probes are available for identifying mitochondria (Dickinson & Chang, 2008; Leung *et al.*, 2013; Rizzuto *et al.*, 1995), they might influence the ongoing iron chemistry and/or lose activity during freeze-drying. Although freeze-drying may induce changes to cells, it is highly unlikely that such complex

Table 2
Surface area analysis and quantitative analysis of iron-rich structures shown in Figs. 2–5.

The first column indicates the manuscript figure to which the data refers. 'Δ (nm)' indicates the resolution of the XRF scan. Surface area analysis and iron quantification were performed based upon manual selection of the pixels belonging to iron-rich structures. The number of pixels, total area (in μm^2) and total number of iron atoms (background-corrected) are provided for each cluster. Mean areal iron concentration of the cluster and the cytosol [c_{areal}(cluster) and c_{areal}(cyt), both in ng cm^{-2}] were calculated from the total number of iron atoms determined and the cluster area. The '$R_{cyt\text{-}Fe}$' column indicates the fraction of the areal iron concentration in the cytosol with respect to the iron hot-spot. 'Pearson (S–Fe)' indicates the Pearson correlation test between the sulfur and iron elemental map. The asterisk (*) indicates that the sample was measured in cryogenic mode and quantified with NIST SRM 1577C instead of AXO thin film.

Figure number	Δ (nm)	No. of pixels	Area (μm^2)	No. of iron atoms	c_{areal} (cluster) (ng cm^{-2})	Mean No. Fe atoms /pixel (cytoplasm)	c_{areal} (cyt) (ng cm^{-2})	$R_{cyt\text{-}Fe}$	Pearson (S–Fe)
Fig. 2(*b*)	20	2737	1.09	4.9×10^6	42	2.3×10^2	5.4	13%	0.3345
Fig. 3(*a*)	20	350	0.14	4.4×10^6	292	4.8×10^2	11.1	4%	0.3468
Fig. 3(*b*)	20	555	0.22	6.1×10^6	257	4.1×10^2	9.5	4%	0.2108
Fig. 3(*c*)	20	668	0.27	2.6×10^6	91	3.7×10^2	8.5	9%	0.0636
Fig. 3(*d*)	30	1633	1.47	2.5×10^6	16	1.2×10^3	12.1	77%	0.1514
Fig. 3(*e*)*	30	1693	1.52	5.7×10^6	35	1.1×10^3	11.7	34%	−0.0416
Fig. 4(*a*)	20	2241	0.90	4.0×10^5	4	4.4×10^1	1.0	25%	0.2023
Fig. 4(*b*)	20	1134	0.45	3.1×10^5	6	5.9×10^1	1.4	22%	0.1491
Fig. 4(*c*)	20	817	0.33	3.3×10^5	9	5.7×10^1	1.3	14%	0.2162
Fig. 4(*d*)(1)	20	352	0.14	1.9×10^5	13	1.5×10^2	3.5	28%	0.1198
Fig. 4(*d*)(2)	20	138	0.06	1.1×10^5	18	1.6×10^2	3.6	20%	
Fig. 4(*d*)(3)	20	261	0.10	1.2×10^5	11	1.6×10^2	3.7	34%	
Fig. 4(*d*)(4)	20	800	0.32	3.2×10^5	9	1.4×10^2	3.2	35%	
Fig. 5(*e*)	20	1041	0.42	5.0×10^5	11	6.4×10^1	1.5	13%	0.1036
Fig. 5(*f*)	20	961	0.38	4.5×10^5	11	5.8×10^1	1.3	12%	0.0854
Fig. 5(*g*)	10	392	0.04	1.6×10^5	39	2.5×10^1	2.3	6%	0.1181
Fig. 6(*g*)	20	1205	0.48	6.3×10^5	12	6.7×10^1	1.5	13%	0.1464
Fig. 6(*h*)	20	1350	0.54	5.9×10^5	10	6.1×10^1	1.4	14%	0.2608
Fig. 6(*i*)	20	734	0.29	4.3×10^5	14	4.1×10^1	1.0	7%	0.1621
Mean			4.8×10^{-1}	1.6×10^6	4.7×10^1	$2{,}6 \times 10^2$	4.5×10^0	20%	0.164
Minimum			3.9×10^{-2}	1.1×10^5	4.1×10^0	$2{,}5 \times 10^1$	9.6×10^{-1}	4%	−0.042
Maximum			1.5×10^0	6.1×10^6	2.9×10^2	$1{,}2 \times 10^3$	1.2×10^1	77%	0.347

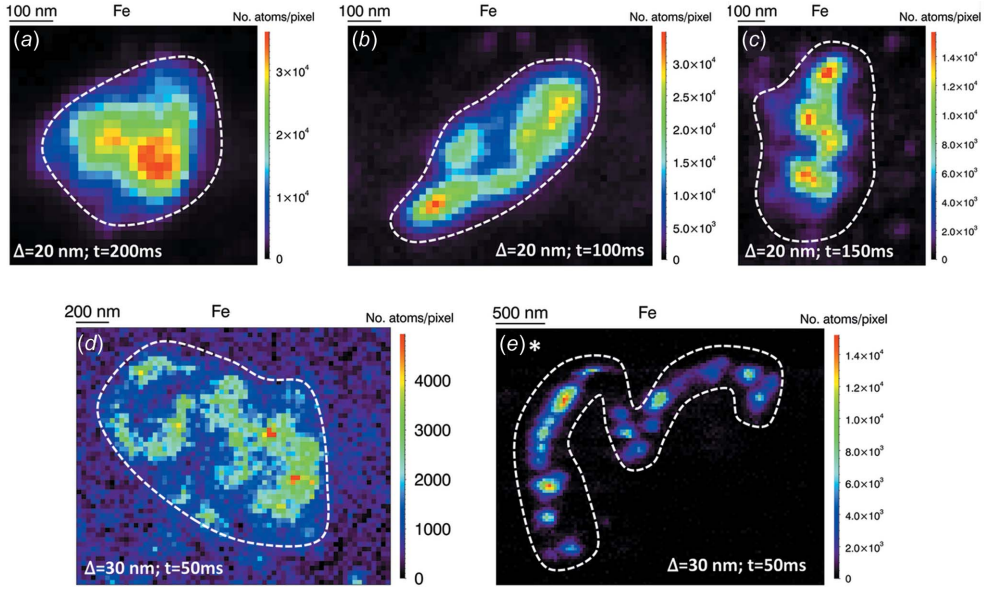

Figure 3
Overview of different iron-rich, (sub)micrometre structures found in other freeze-dried FRDA fibroblasts. (*a*), (*b*), (*c*) Iron-rich structures found within FRDA fibroblasts cultured upon the same silicon nitride membrane and freeze-dried using a commercial freeze-drying instrument. (*d*) Enlargement of the iron-rich structure discussed in Fig. 2(*h*). (*e*) Iron-rich structure found back in a cryogenically frozen fibroblast (also at ID16A beamline, but in cryo-mode). All areal elemental concentrations of iron were background-corrected and are provided as 'No. of atoms/pixel'; quantification for iron was based upon an AXO thin film standard. For quantification of the cryofrozen fibroblast, the K-K_α/K_β ratio of the entire map was used for estimating the approximate ice thickness covering the sample. White dashed lines indicate the area that was used for determining the surface area and the iron areal concentration. For each elemental map, step size (Δ) and dwell time (*t*) are indicated.

recurring iron-rich structure across different cells (and sample wafers) merely represents a sample preparation artifact. In Fig. 3(*e*), a snake-like, mirrored number '3' shape was measured in frozen-hydrated cryofrozen fibroblasts which were measured in earlier work (De Samber *et al.*, 2018). As the iron structure in the FRDA fibroblast shown in Fig. 3(*e*) was measured under cryogenic conditions, the number of iron atoms per pixel calculated was also corrected for additional X-ray absorption caused by the ice covering the fibroblast. Interestingly, after applying absorption correction for the 30 µm ice layer, the concentration range of the color scale bar (expressed in number of atoms/pixel) is comparable with that of the freeze-fried FRDA cells, validating our quantitative calculations across the different synchrotron experiments. Mean surface area and total iron content were determined for all iron structures shown in Fig. 3; the results are summarized in Table 2. The total number of iron atoms varies between two and six million atoms, while the surface area varies from 0.14 to 1.5 µm^2. Also here, little correlation between the sulfur and iron elemental map was found (Pearson correlation coefficient 0.35 or lower). The most likely reason for this is that the relative contrast of sulfur at the location of the iron-rich areas is too small compared with the overall sulfur content in the fibroblasts. From these results we can conclude that SR nano-XRF scanning is able to fairly quickly acquire elemental 'snap-shots' of entire fibroblast cells at medium resolution (400 nm), after which regions of interest (*e.g.* cytosol) or less frequently occurring iron hot-spots can be scanned at higher resolution (50 nm). The total iron content (and area) of iron hot-spots can be estimated as the total number of iron atoms, and spatial correlation with other elemental maps can be performed.

3.2.3. Analysis of iron nanostructures within FRDA fibroblasts. Figs. 4 to 6 summarize the analysis of approximately 15 iron-rich hot-spots located within FRDA fibroblasts. Fig. 3 first shows the areal concentrations of potassium, iron and sulfur within an entire freeze-dried FRDA fibroblast with 50 nm pixel size. In contrast to previous scans shown in Figs. 2 and 3, here a large number of iron hot-spots are located across the fibroblast cytosol, of which seven were re-measured with smaller step sizes of 20 or 10 nm and longer measuring time of 100 ms; results are shown in Figs. 4(*a*)–4(*g*). Mean surface area and total iron content is provided as well in Table 2. The total number of iron atoms ranges from 100000 to 400000 iron atoms, with surface areas from 0.06 to 0.9 µm^2. The Pearson correlation coefficient between the iron and sulfur elemental map did not exceed 0.2, which prevented us from indicating the presence of Fe/S clusters (Maio & Rouault, 2015; Banci *et al.*, 2014; Brancaccio *et al.*, 2014). Generally, iron hot-spots in the fibroblast shown in Fig. 4 seemed to be rather 'stand-alone' events, showing little correlation and revealing little clues on an overall iron architecture within the fibbroblast's cytosol. Fig. 5, on the other hand, shows iron-rich structures in FRDA fibroblasts with a more correlated presence around the nucleus. Fig. 5(*a*) shows light microscopy image of FRDA fibroblasts deposited on the Si_3N_4 membrane, while Fig. 5(*b*) shows an X-ray in-line holographic image of the targeted fibroblast. X-ray in-line holography is an imaging technique in which the phase – reflecting the electron density of the sample – can be reconstructed from propagation-based phase-contrast images taken at different effective propagation distances (Stockmar *et al.*, 2015; Weber *et al.*, 2018; Stockmar *et al.*, 2013; Cloetens *et al.*, 2006). Achievable resolution with in-line holography may vary depending on the sample, but was estimated to be in the 100 nm range for our freeze-dried fibroblast cells. X-ray in-line holographic imaging of a single fibroblast was obtained within 15 min, including phase retrieval, which is significantly less than the time required for 2D nano-XRF imaging upon a single fibroblast (approximately 1–2 h). This makes X-ray phase-contrast imaging an attractive tool for pre-screening the degree of preservation of freeze-dried cells at nanoscopic resolution. Within the fibroblast nucleus [the nuclear membrane is marked with a white dotted line in Figs. 5(*c*) and 5(*d*)], two spherical structures are present which are likely nucleoli. In the corresponding iron elemental map in Fig. 5(*d*), we observe a wealth of iron-containing nanostructures, most of which are confined within a common 'band' [indicated in Figs. 5(*c*) and 5(*d*) with white-dashed lines] in the vicinity of the nucleus. Since the border of this band is not in perfect overlap with the nucleus, it is likely partially above/below it since 2D XRF scanning is only a 'projective' method. The two areas located within the iron-rich band – indicated by 'e' and 'f' in Fig. 5(*d*) – were scanned with smaller step size of 20 nm and longer measuring time of 100 ms, of which the results are provided in Figs. 5(*e*) and 5(*f*). Due to the proximity of the iron-rich band to the nucleus, we believe it is part of the endoplasmic reticulum (ER), where proteins – including iron-containing ones – are assembled. Interestingly, when inspecting the region outside these 'bands' more closely, it turns out not to be completely void but littered with nanoscopic iron-rich 'speckles' [indicated with smaller arrows in Figs. 5(*e*) and 5(*f*)]. Since (iron) background-correction was also applied to Figs. 5(*e*) and 5(*f*), this observation confirms the presence of cytosolic iron, which may be iron present freely in the cytosolic pool, or iron chaperoned by proteins in the labile iron pool (also referred to as LIP). The latter represents chelatable and redox-active iron, which is transitory and serves as a crossroad of cell iron metabolism (Kakhlon & Cabantchik, 2002). Genuinely, the iron 'speckles' observed in Figs. 5(*e*) and 5(*f*) consist of few pixels containing a few thousand atoms each, and therefore likely represent regions of iron chaperoned by iron-chelating proteins. Cytosolic ferritin, a protein which contains in total 4500 iron atoms and has an external diameter of 12 nm (Andrews *et al.*, 1992; Theil, 1987), may be present here. Besides nanoscopic iron-rich 'speckles', larger iron-rich spheres with diameter of approximately 500 nm which are visible in Fig. 5(*d*) – indicated by 'g', 'h' and 'i' – were scanned with 20 nm step size and 400 ms dwell time. The total surface area of the spheres was estimated to be between 0.3 and 0.5 µm^2 (see Table 2), while their total number of iron atoms was estimated to be between 400000 and 600000 atoms. Their spherical shape and relatively small surface area suggests that these could be iron-rich lysosomes, which may explain how the excess of iron in FRDA

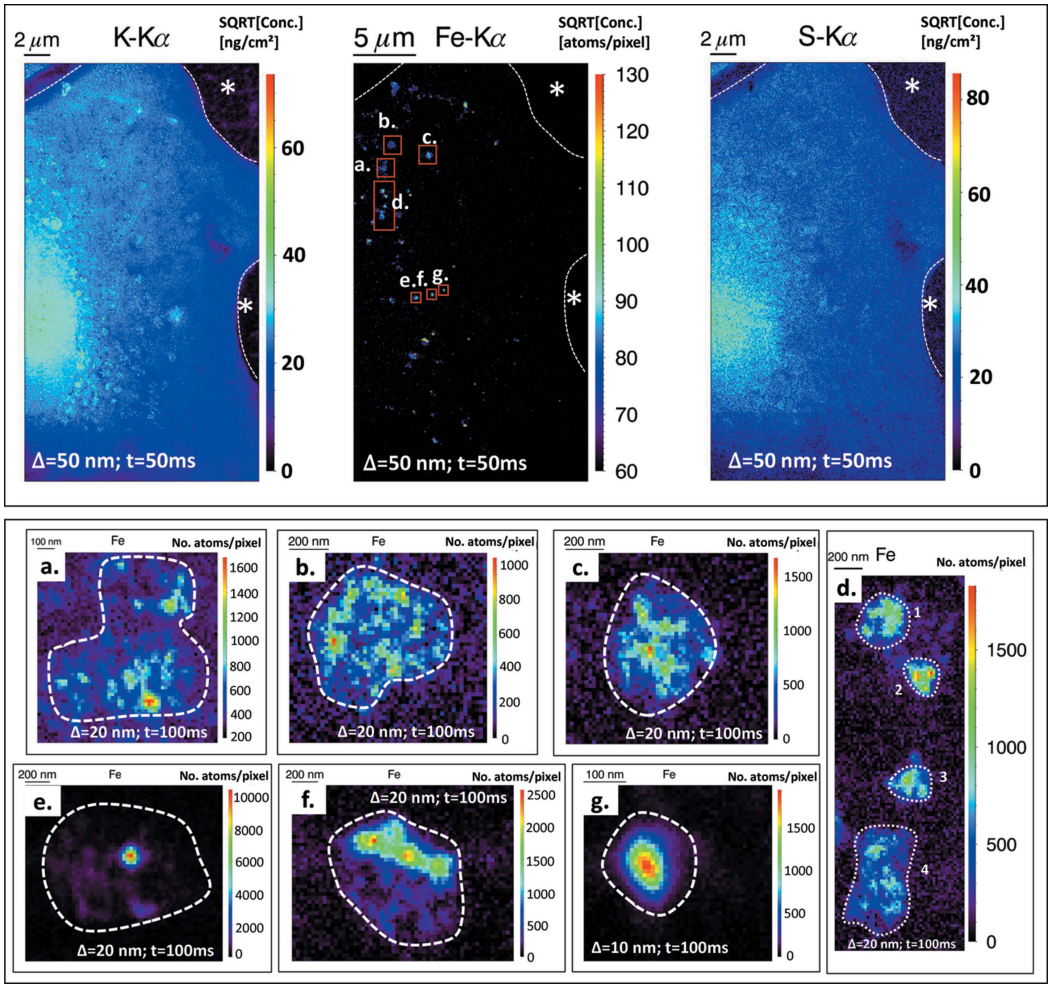

Figure 4
(Upper images) Elemental distributions of potassium, iron and sulfur obtained upon a freeze-dried FRDA fibroblast. All maps were scanned with 50 ms dwell time and have a pixel size of 50 nm. Several iron-rich regions were detected, marked with red rectangles and denoted '*a*' to '*g*'. For clarity, cell boundaries are marked with a white dashed line. For better scaling, areal elemental concentrations of potassium are provided in $(\text{ng cm}^{-2})^{1/2}$, areal elemental concentrations of iron are provided in $[(\text{No. of atoms})/\text{pixel}]^{1/2}$. (Lower images) High resolution (20 nm or 10 nm pixel size) of iron elemental distributions of the iron-rich hot-spots detected. All areal concentrations are background-corrected. The asterisks (*) indicates regions that were used for background subtraction. Areal elemental concentrations of iron are provided in 'No. of atoms/pixel'. White dashed lines indicate the area which was used for determining the surface area and the iron areal concentration. For each elemental map, step size (Δ) and dwell time (*t*) are indicated. Quantification for iron was based upon an AXO thin film standard and upon NIST SRM 1577C for all other elements.

fibroblasts is inactivated and/or removed from the intracellular milieu. Concerning the iron content of the fibroblast cytosol, we could determine that the mean areal iron concentration in the cytosol of FRDA fibroblasts is non-zero after background subtraction, which suggests the presence of a significant portion of iron present in the cytosol. This portion of cytosolic iron – mainly observed as nanoscopic speckles – is likely representative for iron chaperoned in the fibroblast's labile iron pool (Kakhlon & Cabantchik, 2002). Also here, little correlation between iron and sulfur elemental maps was found, not necessarily implying such correlation is not present.

Summarizing, the overall mean surface area of the iron-containing structures was found to be 0.48 μm^2, corresponding to a mean content of 1.6 million iron atoms. Corresponding box plots showing the total number of iron atoms per cluster (*a*), mean iron atoms per pixel (*b*), mean areal iron concentration in iron hot-spot (*c*) and cytoplasm (*d*) are provided in Fig. 6. The ratio between the mean areal concentration of the cytosol with respect to the mean areal concentration of the iron structures '$R_{\text{cyt-Fe}}$' is also shown in Table 2, providing an average value of 20%. Further investigation of iron and sulfur in FRDA fibroblasts could include working on thin (*e.g.* between 500 nm and 2 μm) fibroblast sections, improving contrast for sulfur highly present in entire fibroblasts, or performing fluorescence tomography on whole cells, providing depth resolution for these elements. Nevertheless, analytical capabilities of SR nano-XRF such as determining the average iron content within nanostructures and the mean iron concentration in the cytosol can be considered as major tools in subcellular FRDA research.

4. Conclusion

We imaged, for the first time, iron-containing nanostructures located in the cytoplasm of freeze-dried fibroblasts from Friedreich's ataxia patients using synchrotron-radiation-based

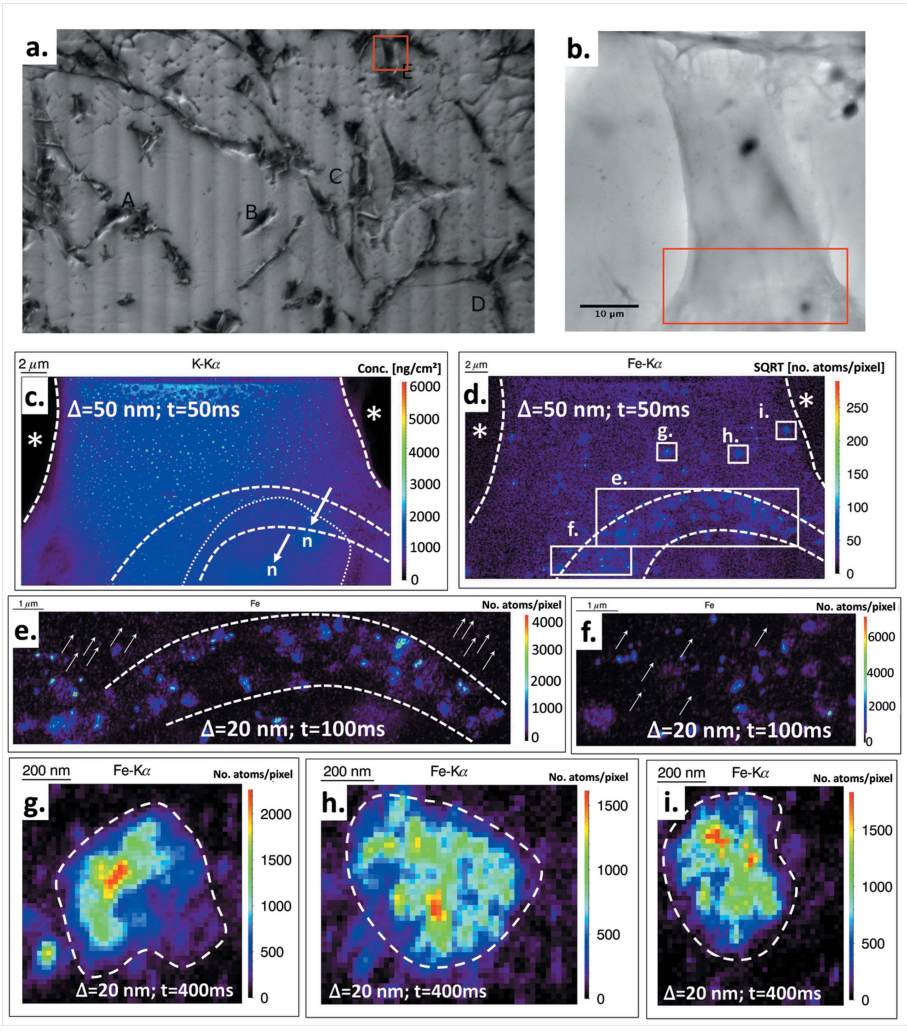

Figure 5
(*a*) Light microscope image of silicon nitride membrane covered with freeze-dried FRDA fibroblasts (the region scanned with in-line holography is indicated with a red rectangle). (*b*) X-ray in-line holography performed upon the fibroblast of interest. The region scanned with SR nano-XRF is indicated with a red rectangle. Field-of-view for each image is 50 µm × 50 µm, scale bar is 10 µm. (*c*) and (*d*) Potassium and iron distribution of a large part of the FRDA fibroblast cytoplasm. Outer white dashed lines indicate the cell border and inner white dashed lines an iron-rich band close to the nucleus. The white dotted line indicates the location of the nuclear membrane; white arrows indicate the presence of two nucleoli. White rectangles (marked 'e' and 'f') indicate two wide iron-rich regions which were scanned at high resolution (20 nm pixel size, 100 ms/pixel), shown in (*e*) and (*f*). White square boxes (marked 'g', 'h' and 'i') indicate three square iron-rich regions also scanned at high resolution (20 nm pixel size, 100 ms/pixel) and shown in (*g*), (*h*) and (*i*). All areal concentrations are background-corrected. The asterisks (*) indicates regions which were used for background subtraction. Areal elemental concentrations of potassium are provided in 'ng cm^{-2}', areal elemental concentrations of iron are provided in 'No. of atoms/pixel'. White dashed lines in (*g*)–(*i*) indicate the area that was used for determining the surface area and the iron areal concentration. Quantification for iron was based upon an AXO thin film standard and upon NIST SRM 1577C for all other elements. For each elemental map, step size (Δ) and dwell time (*t*) are indicated.

nanoscopic XRF, which is currently the spearhead method for nanochemical imaging of trace-level metals within single cells. Freeze-dried cells enabled higher sample throughput and scatter less than their cryofrozen equivalent, causing lower background signal and therefore better limits of detection. Nevertheless, analysis of cryogenically frozen cells can be seen as the method *par excellence* as it represents elemental analysis as close as possible to the *in vivo* state. Using a thin film standard with mass depositions of 1–3 atomic layers (ng mm^{-2} range), we obtained an absolute detection capability of 180 iron atoms under normal scanning conditions, approaching the single-atom level, confirming SR nano-XRF as the ultimate enabling analytical technique for imaging the total iron cellular architecture in whole fibroblasts. In-line X-ray holography was additionally used as a powerful tool for fast morphological imaging of freeze-dried fibroblasts at the 100 nm spatial resolution level. It revealed artifacts of the fibroblast cell structure caused by freeze-drying and ensured a more efficient workflow by pre-selection of cell areas of interest for nano-XRF imaging.

In the close vicinity of the FRDA fibroblasts nucleus, we discovered iron-rich 'bands' spanning tens of micrometres, which are likely part of the endoplasmatic reticulum. Also, we observed micrometre-sized elliptical iron-rich structures with a tubular shape, which likely represent the fibroblast's mitochondria, responsible for various metabolic processes in the cell such as heme synthesis and the electron transport chain (also referred to as 'complex I–IV'). Iron-rich spherical structures – which we located further away from the FRDA fibroblast nucleus – are considered to be iron-containing lysosomes, removing the excess of iron from the intracellular milieu. The mean surface area of all iron-rich structures imaged (considered to be endoplasmatic reticulum, mitochondria or lysosomes) and upon which cluster analysis was feasible amounted to 0.48 µm^2, and contained an average of 1.6 million iron atoms. Interestingly, the fibroblast cytosol turned out to be littered with iron-rich nanoscopic 'speckles', each containing iron atoms in the few-thousand range, which likely represent iron chaperoned by proteins in the fibroblast's labile iron pool. Background-subtracted mean areal cytosolic concentrations amounted to one-fifth of the mean areal concentration of the micrometre-ized iron-rich structures, indicating the presence of a significant portion of cytosolic iron in FRDA fibroblasts. Strong correlation between sulfur and iron elemental distribution in iron hot-spots – which could point out the presence of a so-called iron–sulfur cluster assembly – was not observed, which is likely due to the high

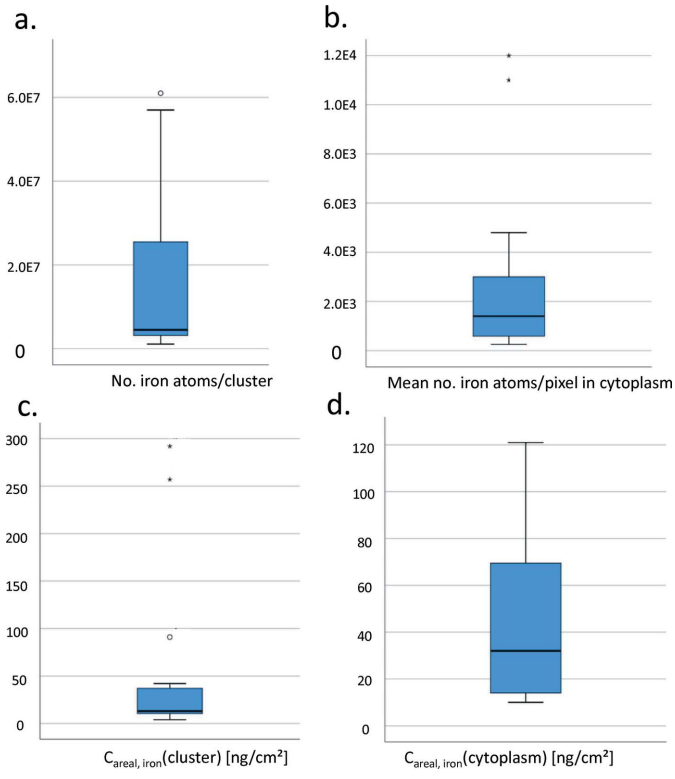

Figure 6
Box plot of (*a*) total number of iron atoms within all iron-rich hot-spots/structures analyzed; (*b*) mean number of iron atoms per pixel in the cytoplasm; (*c*) mean areal concentration of iron in the hot-spots (in ng cm^{-2}); and (*d*) mean areal concentration of iron in the cytoplasm (in ng cm^{-2}).

overall presence of sulfur in the fibroblasts. Further investigation of iron–sulfur correlation in FRDA fibroblasts would require measurements on thin cell sections or performing fluorescence tomography on whole cells.

In summary, our research provided insight into how iron is distributed within a variety of fibroblast organelles, such as the endoplasmatic reticulum, mitochondria and lysosomes, and even within the cytosolic pool. New quantitative insights of iron-rich hot-spots and cytosolic iron within human fibroblasts were obtained. Ultimately, this information can lead to further insight of the metabolic household of iron, involving storage, fabrication and detoxification in FRDA fibroblasts. In order to further unravel the metal architecture and household within single cells at a functional level, coupling of nano-XRF with other state-of-the-art complementary techniques, such as combined cryogenic fluorescence light microscopy and transmission electron microscopy – also referred to as cryogenic correlative light electron microscopy or CLEM – is required (Schaffer *et al.*, 2015). This will enable combined nanochemical and morphological cell imaging, ultimately leading to functional cellular analysis. Seen from a broader perspective, brilliant synchrotron light can as such lift the veil on the amount and complex arrangement of metals at the subcellular scale.

5. Data availability

The ESRF Council has recently endorsed the implementation of a Data Policy for data taken at the ESRF beamlines. The Data Policy is based on the PaNdata Data Policy which was a deliverable of the European FP7 project PaN-data Europe (http://pan-data.eu/) delivered in 2011. The Data Policy defines the ESRF as the custodian of raw data and metadata. The metadata is stored in the ICAT metadata catalog (https://icatproject.org/) which can be accessed online (https://icat.esrf.fr) to browse and download (meta)data. A three-year embargo period applies after each ESRF measurement during which the experimental team has the right to have sole access to the data, renewable if necessary. The (meta)data related to the experiment of this manuscript (LS-2657) will be released entirely in May 2020 under a CC-BY-4 license with open access to anyone who has registered with the ESRF data portal.

Acknowledgements

The authors acknowledge the ID16A 'Nano-Imaging' beamline staff for help and support during the measurements. They would also like to thank the Department of Chemistry and the Department of Pharmaceutical Sciences at Ghent University for kindly providing the freeze-drying equipment.

Funding information

The following funding is acknowledged: Fonds Wetenschappelijk Onderzoek (bursary No. 12B3313N to BDS); European Synchrotron Radiation Facility (experiment No. LS-2657).

References

Adamec, J., Rusnak, F., Owen, W. G., Naylor, S., Benson, L. M., Gacy, A. M. & Isaya, G. (2000). *Am. J. Hum. Genet.* **67**, 549–562.
Andrews, N. C. (2008). *Blood*, **112**, 219–230.
Andrews, S. C., Arosio, P., Bottke, W., Briat, J. F., von Darl, M., Harrison, P. M., Laulhère, J. P., Levi, S., Lobreaux, S. & Yewdall, S. J. (1992). *J. Inorg. Biochem.* **47**, 161–174.
Banci, L., Brancaccio, D., Ciofi-Baffoni, S., Del Conte, R., Gadepalli, R., Mikolajczyk, M., Neri, S., Piccioli, M. & Winkelmann, J. (2014). *Proc. Natl Acad. Sci. USA*, **111**, 6203–6208.
Beinert, H., Holm, R. H. & Münck, E. (1997). *Science*, **277**, 653–659.
Bencze, K. Z., Kondapalli, K. C., Cook, J. D., McMahon, S., Millán-Pacheco, C., Pastor, N. & Stemmler, T. L. (2006). *Crit. Rev. Biochem. Mol. Biol.* **41**, 269–291.
Bencze, K. Z., Yoon, T., Millán-Pacheco, C., Bradley, P. B., Pastor, N., Cowan, J. A. & Stemmler, T. L. (2007). *Chem. Commun.* pp. 1798–1800.
Brancaccio, D., Gallo, A., Mikolajczyk, M., Zovo, K., Palumaa, P., Novellino, E., Piccioli, M., Ciofi-Baffoni, S. & Banci, L. (2014). *J. Am. Chem. Soc.* **136**, 16240–16250.
Bulteau, A. L., O'Neill, H. A., Kennedy, M. C., Ikeda-Saito, M., Isaya, G. & Szweda, L. I. (2004). *Science*, **305**, 242–245.
Cagno, S., Brede, D. A., Nuyts, G., Vanmeert, F., Pacureanu, A., Tucoulou, R., Cloetens, P., Falkenberg, G., Janssens, K., Salbu, B. & Lind, O. C. (2017). *Anal. Chem.* **89**, 11435–11442.
Cavadini, P., O'Neill, H. A., Benada, O. & Isaya, G. (2002). *Hum. Mol. Genet.* **11**, 217–227.
Chen, S., Deng, J., Yuan, Y., Flachenecker, C., Mak, R., Hornberger, B., Jin, Q., Shu, D., Lai, B., Maser, J., Roehrig, C., Paunesku, T., Gleber, S. C., Vine, D. J., Finney, L., VonOsinski, J., Bolbat, M.,

Spink, I., Chen, Z., Steele, J., Trapp, D., Irwin, J., Feser, M., Snyder, E., Brister, K., Jacobsen, C., Woloschak, G. & Vogt, S. (2014). *J. Synchrotron Rad.* **21**, 66–75.
Cloetens, P., Mache, R., Schlenker, M. & Lerbs-Mache, S. (2006). *Proc. Natl Acad. Sci. USA*, **103**, 14626–14630.
Cook, J. D., Bencze, K. Z., Jankovic, A. D., Crater, A. K., Busch, C. N., Bradley, P. B., Stemmler, A. J., Spaller, M. R. & Stemmler, T. L. (2006). *Biochemistry*, **45**, 7767–7777.
De Samber, B., Meul, E., Laforce, B., De Paepe, B., Smet, J., De Bruyne, M., De Rycke, R., Bohic, S., Cloetens, P., Van Coster, R., Vandenabeele, P. & Vanden Berghe, T. (2018). *PLoS One*, **13**, e0190495.
De Samber, B., Niemiec, M. J., Laforce, B., Garrevoet, J., Vergucht, E., De Rycke, R., Cloetens, P., Urban, C. F. & Vincze, L. (2016). *PLoS One*, **11**, e0165604.
Dickinson, B. C. & Chang, C. J. (2008). *J. Am. Chem. Soc.* **130**, 9638–9639.
Fakih, S., Podinovskaia, M., Kong, X., Schaible, U. E., Collins, H. L. & Hider, R. C. (2009). *J. Pharm. Sci.* **98**, 2212–2226.
Fus, F., Yang, Y., Pacureanu, A., Bohic, S. & Cloetens, P. (2018). *Opt. Express*, **26**, 32847–32865.
Gramaccioni, C., Yang, Y., Procopio, A., Pacureanu, A., Bohic, S., Malucelli, E., Iotti, S., Farruggia, G., Bukreeva, I., Notargiacomo, A., Fratini, M., Valenti, P., Rosa, L., Berlutti, F., Cloetens, P. & Lagomarsino, S. (2018). *Appl. Phys. Lett.* **112**, 053701.
Hassannia, B., Wiernicki, B., Ingold, I., Qu, F., Van Herck, S., Tyurina, Y. Y., Bayır, H., Abhari, B. A., Angeli, J. P. F., Choi, S. M., Meul, E., Heyninck, K., Declerck, K., Chirumamilla, C. S., Lahtela-Kakkonen, M., Van Camp, G., Krysko, D. V., Ekert, P. G., Fulda, S., De Geest, B. G., Conrad, M., Kagan, V. E., Vanden Berghe, W., Vandenabeele, P. & Vanden Berghe, T. (2018). *J. Clin. Invest.* **128**, 3341–3355.
Herrera, R., Álvarez, M. C., Gelis, S. & Ramos, J. (2013). *Biochem. J.* **454**, 525–532.
Imoto, S., Kono, M., Suzuki, T., Shibuya, Y., Sawamura, T., Mizokoshi, Y., Sawada, H., Ohbuchi, A. & Saigo, K. (2018). *Transfus. Apher. Sci.* **57**, 524–531.
Jin, Q. L., Paunesku, T., Lai, B., Gleber, S. C., Chen, S., Finney, L., Vine, D., Vogt, S., Woloschak, G. & Jacobsen, C. (2017). *J. Microsc.* **265**, 81–93.
Johnson, D. C., Dean, D. R., Smith, A. D. & Johnson, M. K. (2005). *Annu. Rev. Biochem.* **74**, 247–281.
Kakhlon, O. & Cabantchik, Z. I. (2002). *Free Radical Biol. Med.* **33**, 1037–1046.
Koeppen, A., Ramirez, R., Bjork, S., Mazurkiewicz, J. & Kuntzsch, E. (2013). *J. Neuropathol. Exp. Neurol.* **72**, 554.
Koeppen, A. H. (2011). *J. Neurol. Sci.* **303**, 1–12.
Koeppen, A. H., Ramirez, R. L., Yu, D., Collins, S. E., Qian, J., Parsons, P. J., Yang, K. X., Chen, Z. W., Mazurkiewicz, J. E. & Feustel, P. J. (2012). *Cerebellum*, **11**, 845–860.
Kruger, P. C., Yang, K. X., Parsons, P. J., Becker, A. B., Feustel, P. J. & Koeppen, A. H. (2016). *Am. J. Cardiol.* **118**, 127–131.
Kurz, T., Terman, A., Gustafsson, B. & Brunk, U. T. (2008). *Biochim. Biophys. Acta*, **1780**, 1291–1303.
Lackner, L. L. (2013). *Curr. Opin. Cell Biol.* **25**, 471–476.
Lamarche, J. B. C. M., Côté, M. & Lemieux, B. (1980). *Can. J. Neurol. Sci.* **7**, 389–396.
Lesuisse, E., Santos, R., Matzanke, B. F., Knight, S. A. B., Camadro, J. M. & Dancis, A. (2003). *Hum. Mol. Genet.* **12**, 879–889.
Leung, C. W. T., Hong, Y. N., Chen, S. J., Zhao, E. G., Lam, J. W. Y. & Tang, B. Z. (2013). *J. Am. Chem. Soc.* **135**, 62–65.
Li, Q., Han, X., Lan, X., Gao, Y., Wan, J., Durham, F., Cheng, T., Yang, J., Wang, Z., Jiang, C., Ying, M., Koehler, R. C., Stockwell, B. R. & Wang, J. (2017). *JCI Insight*, **2**, e90777.
Llorens, J. V., Soriano, S., Calap-Quintana, P., Gonzalez-Cabo, P. & Moltó, M. D. (2019). *Front. Neurosci.* **13**, 75.
Ma, Y., Abbate, V. & Hider, R. C. (2015). *Metallomics*, **7**, 212–222.
Maio, N. & Rouault, T. A. (2015). *Biochim. Biophys. Acta*, **1853**, 1493–1512.
Mühlenhoff, U., Hoffmann, B., Richter, N., Rietzschel, N., Spantgar, F., Stehling, O., Uzarska, M. A. & Lill, R. (2015). *Eur. J. Cell Biol.* **94**, 292–308.
Ramirez, R. L., Qian, J., Santambrogio, P., Levi, S. & Koeppen, A. H. (2012). *Am. J. Cardiol.* **110**, 1820–1827.
Richardson, D. R., Lane, D. J. R., Becker, E. M., Huang, M. L. H., Whitnall, M., Rahmanto, Y. S., Sheftel, A. D. & Ponka, P. (2010). *Proc. Natl Acad. Sci. USA*, **107**, 10775–10782.
Rizzuto, R., Brini, M., Pizzo, P., Murgia, M. & Pozzan, T. (1995). *Curr. Biol.* **5**, 635–642.
Rötig, A., de Lonlay, P., Chretien, D., Foury, F., Koenig, M., Sidi, D., Munnich, A. & Rustin, P. (1997). *Nat. Genet.* **17**, 215–217.
Schaffer, M., Engel, B. D., Laugks, T., Mahamid, J., Plitzko, J. M. & Baumeister, W. (2015). *Bio-Protocol*, **5**, e1575.
Scharlach, C., Müller, L., Wagner, S., Kobayashi, Y., Kratz, H., Ebert, M., Jakubowski, N. & Schellenberger, E. (2016). *J. Biomed. Nanotechnol.* **12**, 1001–1010.
Silva, J. C. da, Pacureanu, A., Yang, Y., Bohic, S., Morawe, C., Barrett, R. & Cloetens, P. (2017). *Optica*, **4**, 492–495.
Stockmar, M., Cloetens, P., Zanette, I., Enders, B., Dierolf, M., Pfeiffer, F. & Thibault, P. (2013). *Sci. Rep.* **3**, 1927.
Stockmar, M., Hubert, M., Dierolf, M., Enders, B., Clare, R., Allner, S., Fehringer, A., Zanette, I., Villanova, J., Laurencin, J., Cloetens, P., Pfeiffer, F. & Thibault, P. (2015). *Opt. Express*, **23**, 12720–12731.
Theil, E. C. (1987). *Annu. Rev. Biochem.* **56**, 289–315.
Valko, M., Morris, H. & Cronin, M. T. D. (2005). *Curr. Med. Chem.* **12**, 1161–1208.
Vekemans, B., Janssens, K., Vincze, L., Adams, F. & Van Espen, P. (1994). *X-ray Spectrom.* **23**, 278–285.
Weber, L., Hänsch, A., Wolfram, U., Pacureanu, A., Cloetens, P., Peyrin, F., Rit, S. & Langer, M. (2018). *J. Microsc.* **269**, 36–47.
Wiemerslage, L. & Lee, D. (2016). *J. Neurosci. Methods*, **262**, 56–65.
Yang, Y., Fus, F., Pacureanu, A., da Silva, J. C., De Nolf, W., Biot, C., Bohic, S. & Cloetens, P. (2019). *Anal. Chem.* **91**, 6549–6554.